Microstructure-magnetic shielding development in additively manufactured Ni-Fe-Mo soft magnet alloy in the as fabricated and post-processed conditions

Hussein, Abdelmoez; Attallah, Moataz; Sheridan, Richard; Bongs, Kai

DOI:
10.1016/j.jallcom.2021.161112

Document Version
Peer reviewed version

Citation for published version (Harvard):
Hussein, A, Attallah, M, Sheridan, R & Bongs, K 2021, 'Microstructure-magnetic shielding development in additively manufactured Ni-Fe-Mo soft magnet alloy in the as fabricated and post-processed conditions', *Journal of Alloys and Compounds*, vol. 884, 161112. https://doi.org/10.1016/j.jallcom.2021.161112

Microstructure-Magnetic Shielding Development in Additively Manufactured Ni-Fe-Mo Soft Magnet Alloy in the As-Fabricated and Post-Processed Conditions

Abd El-Moez A. Mohamed[a], R. S. Sheridan[a], Kai Bongs[b], Moataz M. Attallah[*a]

[a] School of Metallurgy and Materials, University of Birmingham, B15 2TT, Birmingham, United Kingdom

[b] School of Physics and Astronomy, University of Birmingham, B15 2TT, Birmingham, United Kingdom

Abstract

This study introduces a deep analysis, which correlates the metallurgical characters with the magnetic properties in laser powder bed fusion processed Ni-Fe-Mo, to produce 3D prototypes with maximum magnetic shielding performance for ultra-sensitive quantum-based systems. The study conducts a sequenced plan of optimising the magnetic properties via microstructure density control, controlling the magnetic anisotropy, before applying heat treatment (HT) and hot isostatic pressing (HIP) post-processes. This is also considering delivering effective mechanical properties. The magnetic properties optimisation was performed via laser parametric study, which found that the sample built with laser energy density E=4.68J/mm^2 achieves the best soft magnetic and mechanical results due to the lowest defects. However, the obtained magnetic properties are still poor, due to the (001) rich grain orientation, which parallels the hard axis of magnetisation <100> in this alloy. It was found that tilting the crystallographic orientation of the as fabricated (AF) optimised condition with 45˚ and 35˚, with respect to the build direction, improves the soft magnetic properties, as these angles correspond to the easy axes of magnetisation <110> and <111>, respectively, allowing the grain orientation in the same directions. The magnetic properties are further promoted with HT and HIP post-processes application. The magnetic shielding results of hollow tubes, built with the same optimised condition, confirmed the magnetic behaviour of the bulk coupons, achieving 83% of the commercial magnetic shielding.

Keywords: Mu-metal; Magnetic properties; Magnetic shielding; Microstructure; laser powder bed fusion.

[*]**Corresponding author: M.M.Attallah (m.m.attallah@bham.ac.uk)**

1. Introduction

Magnetic shielding is an important technology, which provides a suitable magnetic environment for ultra-sensitive quantum-based systems, such as cold atom sensors [1] and quantum gravity sensors [2], which can be easily perturbed by the magnetic field of the earth (50μT). Several magnetic materials have been investigated as passive magnetic shields; however, Mu-metal ($Ni_{80}Fe_{15}Mo_5$) has been shown to be the most effective candidate [3], due to its low coercivity (H_c) and high permeability [4], which are the most important characteristics of promising passive magnetic shields. Efforts have been paid for 3D printing of magnetic shields using additive manufacturing techniques [1], which are somewhat limited by conventional processing methods. $Ni_{80}Fe_{20}$ (Permalloy-80) and Mu-metal have been investigated using laser powder bed fusion (LPBF) additive manufacturing technique in several works [1,5, 6], however, the magnetic properties were poor (H_c values are high) due to the induced anisotropy and microstructural defects [4]. The crystallographic anisotropy in LPBF processed materials is a dependent factor on laser energy input [7], where several studies have confirmed the [100] direction as a preferred grain orientation/texture for the LPBF processed Ni-based alloys; the direction of the hard magnetisation axis within these alloys [6, 8]. The higher cooling rate during the LPBF process results in residual stresses [9], fine grains [10] and microstructural defects (such as cracks, holes and dislocations), which suppress the magnetic properties via magnetic domain walls pining [11]. Therefore, most published studies have focused only on optimising laser-processing parameters for high-quality dense samples, though some studies reported texture and grain orientation control [6]. However, Vovroch et al. [1] and Mohamed et al. [4] reported outstanding results for LPBF processed Mu-metal magnetic shields components, which may be a benchmark in additive manufactured magnetic shields technology. The current study introduces an analysis, which correlates the microstructural characteristics with the magnetic properties in LPBF Mu-metal, to produce 3D printed

magnetic shields prototypes with maximum performance. This is conducted in a sequenced plan of optimising the magnetic properties of bulk coupons via laser parametric study, changing the magnetic anisotropy of the optimised condition via controlling the crystallographic orientation, applying post-processes, testing the idea on a real prototype and measuring the magnetic shielding effect. This is also considering delivering effective mechanical properties.

2. Experimental and methods

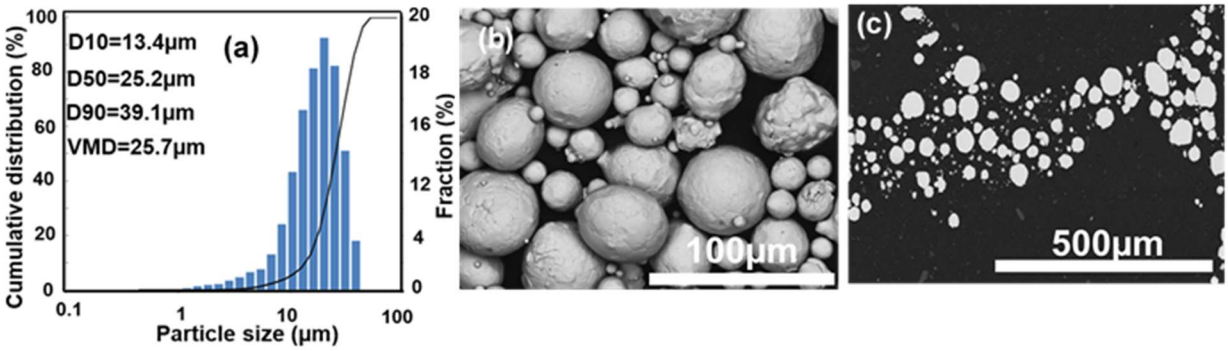

Fig.1: (a) Particle size distribution and (b,c) SEM micrographs of the raw pre-alloyed powder and its cross-sectional view of polished particles, respectively.

Table 1: chemical composition (Wt%) of the raw pre-alloyed powder, AF and HT bulk coupons built with E=4.68J/mm²

	Fe	Mo	O	Si	Mn	Co	Cr	Ni
Powder	12.8	4.37	0.038	0.02	<0.02	<0.02	<0.02	Bal
AF bulk	14.21	4.67	0.042	<0.02	<0.02	<0.02	<0.02	Bal
HT	14.56	4.81	0.026	<0.02	<0.02	<0.02	<0.02	Bal

Mu-metal pre-alloyed powder (ASTM A753 Alloy4) with chemical composition listed in Table 1 was provided by Erasteal. The particle size distribution was performed using a laser Sympatec particle size analyser and shows a volume main diameter (VMD) value of 25.7µm as shown in Fig.1a. The scanning electron microscope (SEM) micrographs in Fig.1b,c shows the powder morphology and the cross-sectional view of polished particles, respectively. The particles are spherical with few satellites on top (See Fig. 1b) and fully dense without any evidence of gas trapped pores (during the atomisation process), as seen in Fig.1c. The raw powder was processed by the LPBF technique, using a Concept laser M2 Cusing system, as detailed in Ref [6].

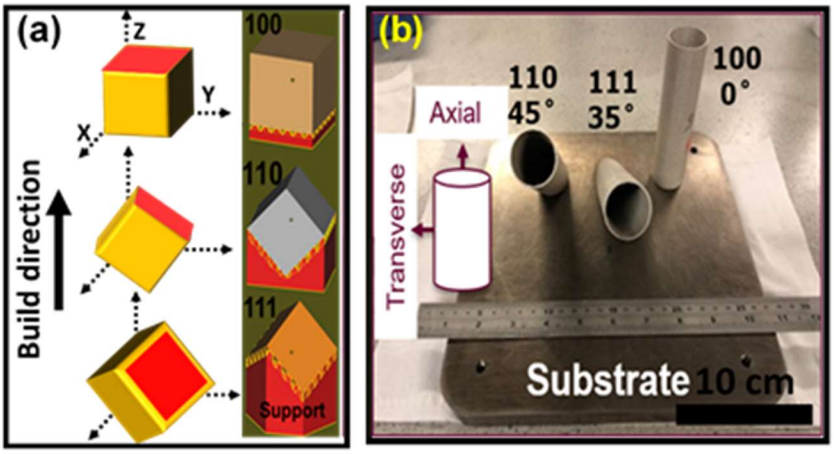

Fig.2: Sample build orientation of AF 100, 110 and 111 bulk (a) coupons and (b) hollow tubes.

The laser parametric study was performed on untilted 10x10x10mm^3 bulk coupons, 0˚ with respect to the build direction (YZ) (100 orientation), using processing window parameters of 150-300W laser power (P), 800-3500mm/s scan speed (v), 0.03-0.09mm laser hatch space (h) and a constant layer thickness of 30µm on top of nickel substrate. The processing parameter combination was expressed in terms of the energy density model (E), which is given by the equation E=P/v.h [12]. The optimised condition was used to build coupons and hollow tubes with tilted crystallographic orientation 45˚ and 35˚, with respect to the build direction, as shown in Fig.2. The AF 100 samples have a strong (100) texture along the build direction, therefore tilting coupons with 45° and 35° (as seen in Fig.2a) is expected to tilt texture orientation in the [110] and [111], the easy magnetization directions [4,6]. All primary microstructure and magnetic optimisation investigations were performed on the bulk coupons before the results were applied to the hollow tubes (outer diameter=30 mm, length=140 mm and thickness=1 mm), designed especially for the magnetic shielding measurements. Post-processes HT and HIP combination were applied on four groups of the AF 100, 110 and 111 oriented coupons and tubes. The first group was HTed in Hydrogen atmosphere at 1150˚C for four hours according to the HT protocol reported in Ref [4]. The second group was HIPed at 1230˚C and 120 MPa for three hours (simultaneous application of pressure and temperature, with the

temperature, ramped up and down 5˚C/min). The third group was HT then HIP treated (HT+HIP), while the fourth group was HIP treated followed by HT (HIP+HT).

The samples were cut from the substrate using an electrical discharge machine (EDM), where the AF 100 coupons were then sectioned along the build direction and prepared for the microstructure characterisation following the protocol reported in Ref [6]. The microstructure's characterisation was carried out on a polished surface using a Brunel optical microscope, Hitachi TM3000 scanning electron microscopy (SEM) and a PHILIPS XL30 SEM equipped with electron backscattering diffraction (EBSD). The porosity fraction was estimated from the optical microscope image analysis via Image J software, each porosity data is an average of 9-image analysis. The crystal structure was examined using the x-ray diffraction (XRD) technique (Panalytical Empyrean in a Bragg-Brentano geometry fitted with a Co-tube (K_α radiation, λ=1.79Å)) at room temperature. Crystal structure analysis was performed via Rietveld refinement using FullProf software. The XRD was performed in the first round of optimisation of the AF 100 oriented coupons on the XY direction, then on the red highlighted plane in the tilted coupons as seen in Fig. 2a. Microhardness measurements were performed along the BD using a Wilson VH1102-1202 microhardness tester, where each data point is an average of 16 readings. The magnetic hysteresis loops were measured at room temperature using a LakeShore 7300 vibrating sample magnetometer, considering the demagnetisation factor, and the applied magnetic field in parallel with the build direction. The used magnetic field step size is ≈ 160A/m only around the origin (from the applied magnetic field of -0.21792x10^5A/m to 0.21333x10^5A/m). The magnetisation dependent temperature measurements were performed from room temperature to 600 ºC under magnetic field of 0.05T. The magnetic shielding measurements were performed on the hollow built tubes using a Bartington Mag-13 MC magnetic probe equipped with a Helmholtz coil, with an externally applied magnetic flux density of 50μT. The magnetic shielding measurements were performed

in two directions: the axial direction, where the applied magnetic field is parallel to the tube axis, and the transversal direction, where the applied magnetic field direction is perpendicular to the tube axis (See Fig.2b), as reported in [4]. The magnetic shielding factor (SF) was estimated as the ratio between the external applied magnetic flux density (B_{out}) to the magnetic flux density inside the tube B_{in} (shielded part), according to the equation $SF=B_{out}/B_{in}$ [13]. Where the maximum commercially achieved SF for the Mu-metal is around 600 (magnetic shielding limited 2019, personal communication, 03 Octobre 2019).

3. Results and discussion

3.1 Influence of process parameters on the AF 100 builds

3.1.1 Microstructure

Fig.3a shows the XRD patterns for some selected AF 100 samples processed with various E, which covers all the studied range. Rietveld refinement of the XRD patterns shows the cubic structure for all samples with Fm3m symmetry, the refinement goodness of fitting factor (χ^2) is $1.05 \leq \chi^2 \leq 2.15$ and the powder refinement profile is presented in Fig.3b as an example. The powder XRD pattern in Fig.2a shows higher (111) peak intensity (I_{111}), where (111) is the preferred orientation as the easy axis magnetisation for Mu-metal [6]. The I_{111} peak is annihilated in the consolidated samples with the increase in E, and instead, the samples show a strong (100) texture, which is the preferred orientation during the solidification process, and is parallel with the build direction [4, 6]. The change in peak intensities reveals a strong dependence of crystallographic anisotropy on E [4, 14]. The increase in E induces internal residual stresses, which is common in LPBF process due to the higher local temperature gradient during the build process [15-17], which explains the expansion in crystal lattice cell parameters (see Fig.3c) [18].

The optical micrographs of the AF 100 samples in Fig. 4a show the promotion in the microstructure's density (as a function of porosity fraction) with increasing E. The impact of E on consolidation behaviour agrees with previously published works on Ni-superalloys [12] and

NiFe-based alloys [5, 6]. Fig.4a not only shows the change in defect levels with E, but also shows the change in defect types. There are three types of E-dependent defects observed throughout this study's range of E: lack of fusion defect/un-melted particles entrapped within the pores, microcracks and keyholes. The lack of fusion defect occurs in the samples built with

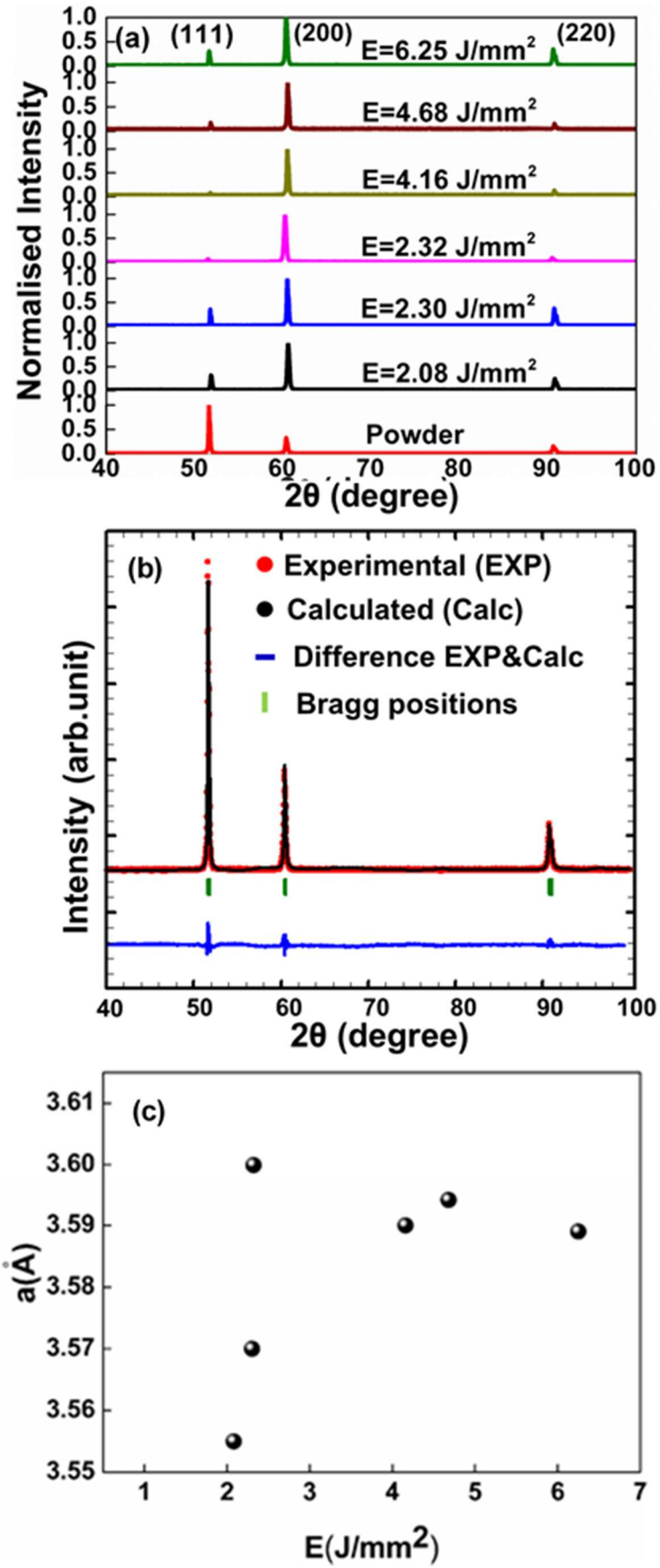

Fig.3: (a) XRD patterns of the AF 100 LPBF-processed Ni-Fe-Mo with different energy densities, (b) Rietveld refinement profile of powder and (c) the change in crystal lattice cell parameter with E.

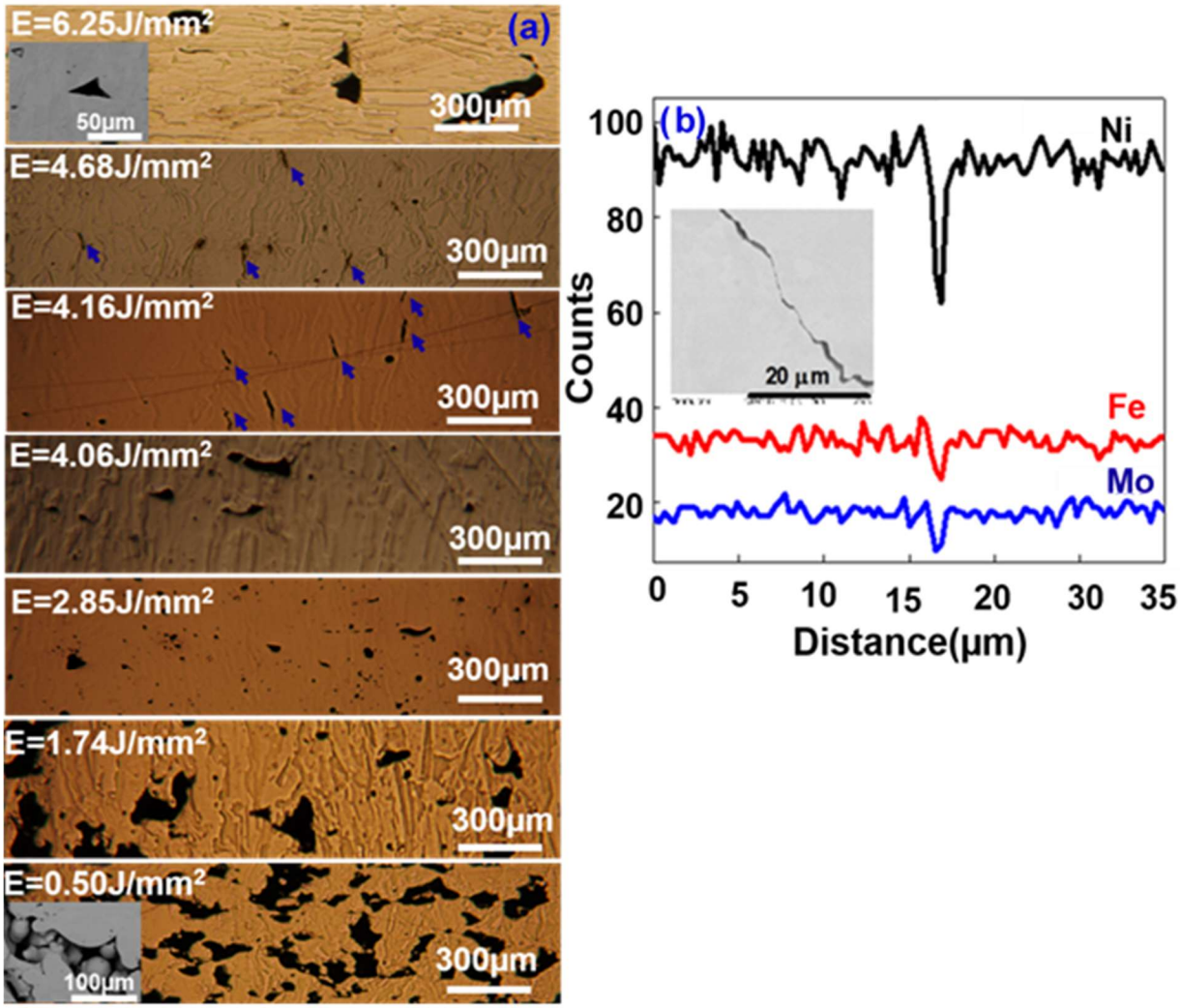

Fig. 4: (a) Optical micrographs of the AF 100 samples orientation with different E conditions along build direction, and (b) EDS line scan across the inset microcrack.

E <1 J/mm^2 (see inset Fig.4a), which normally happens due to the insufficient E, leading to low microstructural density [12]. The lack of fusion defects decreases gradually with the increase in E, until the coexistence of microcracks, as pointed by the arrows, and the small fraction of voids at E=4.16 J/mm^2; both are high E defects [6]. The cracks grow longitudinally, with the build direction, commonly observed in LPBF Ni-based alloys and attributed to the residual stress and ductility reduction caused due to higher cooling rates [16,17]. Cracks can arise from elemental segregation at grain boundaries, breaking grains and interrupting the chemical composition in this position (see Fig.4b) and weakening material strength [17, 19]. At higher levels of E (E>4.68J/mm^2), voids/keyholing are dominant due to the higher

evaporation rates in the melting pool, which creates pores within the build [20]. The AF 100 sample built with E=4.68 J/mm^2 shows the lowest voids and cracks, which can be easily eliminated by the HIP post-process.

3.1.2 Magnetic properties

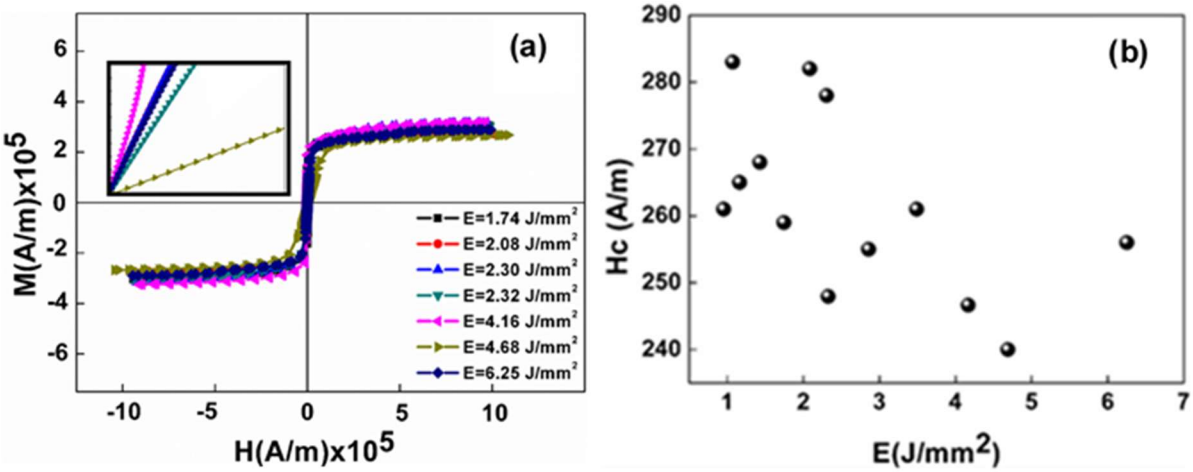

Fig 5.(a) Hysteresis loops of some selected AF 100 samples orientation with different E conditions and the inset represent a high magnification around the origin in the positive quartile and (b) the variation of Coercivity of the AF 100 samples built with different E conditions.

Fig.5a shows the room temperature hysteresis loops of the AF 100 oriented samples with different E conditions. The samples show an insignificant change in the saturation magnetisation (M_s) as they have the same chemical composition. Meanwhile, the inset shows a change in the initial magnetisation slope with changing E, meaning that their magnetisation saturated at different values of the magnetic field, revealing a change in magnetic anisotropy with E [4]. The H_c was determined from the magnetic hysteresis loops, with its behaviour with E presented in Fig.5b. The H_c values decrease with the increase in E, with a minimum value of 242 A/m, which is proportional with E, in agreement with previous studies of LPBF processed Mu-metal [6]. The E dependence of H_c can be interpreted according to the change within the microstructural properties. Coercivity in magnetic materials arises from the free movement of the internal magnetic domain walls [21], which is affected by the induced microstructural defects (pores, cracks and un-melted particles) during the LPBF process [11, 22]. This occurs

via magnetic domain wall pinning, which impedes domain wall movement during the magnetisation and demagnetisation processes [22, 23]. This explains the improvement in the microstructural density and the soft magnetic properties with an increase in E. The minimum value of H_c is found at the sample built with E=4.68 J/mm^2 with the lowest defects. In a comparison with previous research on LPBF of pre-alloyed Mu-metal powder, the H_c values in this study are close to that reported by Li et al. (198 A/m) in $Ni_{78.8}Fe_{15.35}Mo_{4.5}$ [24]. But, Zuo et al. reported much lower H_c (76 A/m), that could be due to higher Fe and O content in their starting Mu-metal powder ($Ni_{77.33}Fe_{16.43}Mo_{5.94}$) [6]. However, they are significantly lower than the values reported by Mikler et al and Zhang et al. (2387 A/m and 390 A/m, respectively) for $Ni_{30}Fe_{70}$ and $Ni_{80}Fe_{20}$ alloys, respectively, which are employed from blended powder using laser engineered net shaping and LPBF techniques [5, 25]. The great difference in values from Refs [5, 25] refers to the starting pre-alloyed powder and the different chemical composition, which provides better homogeneity and fewer defects, therefore, leads to better magnetic properties. It is worth mentioning that the cast permalloy-80 show extremely low H_c values (0.39 A/m and 2.3 A/m) [26] due to the lower cooling rates, which leads to lower defects and larger grains in comparison with the LPBF process [24].

3.1.3 Microhardness

Fig.6 shows the average values of the microhardness Vickers (HV) dependent E for the AF 100 samples. The HV values increase monotonically with the increase in E, showing a constant average value of 230HV at E≥2.30 J/mm^2, in agreement with previously published works of LPBF processed Fe-Ni-Si [27] and A357 Al [28]. The strong dependence of the hardness on E is attributed to the improvement in the microstructural density [29]. In other words, the increase in E increases the melting pool size, which decreases the tendency of pores formation [30]. The maximum achieved microhardness values of the AF samples are consistent

with LPBF processed Mu-metal (228HV) [24], 316L stainless steel (239 HV) [31] and are significantly higher than the cold-rolled $Ni_{48}Fe_{52}$ alloy (100 HV)[32].

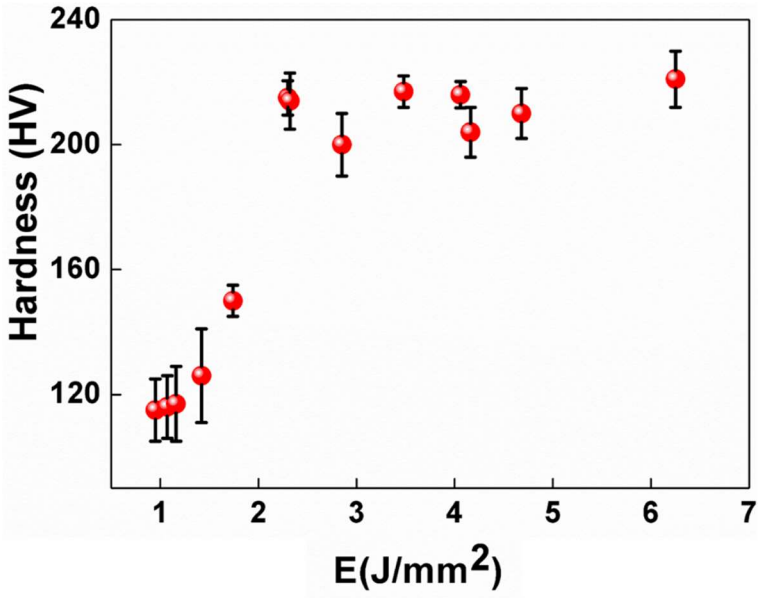

Fig. 6: Average microhardness vs. E along the build direction of the AF 100 samples.

However, the values are lower than the wrought and LPBF processed Ni-superalloys (323 HV) [33].

3.2 Influence of crystallographic anisotropy and post-process on microstructure and magnetic properties

3.2.1 Texture

The sample built with E=4.68J/mm^2 both shows effective magnetic and mechanical properties, meaning this will be used for further investigations. Fig. 7a shows the normalised XRD patterns for the AF 100, 110 and 111 oriented coupons. Tilting the crystallographic build orientation in the [110] and [111] directions results in a significant increase in the I_{111}, which indicates the seldom (100) texture in these directions in agreement with [6]. Furthermore, the I_{111} is further promoted with HIP and HT post-processes in all build orientations, as seen in Fig.7b,c,d. This is a result of improvements in the microstructure due to thermal treatment. For example, HT decreases the residual stresses, dislocation density and inclusions induced during the LPBF process [34], and the HIP collapses the residual microcracks/pores, increasing the

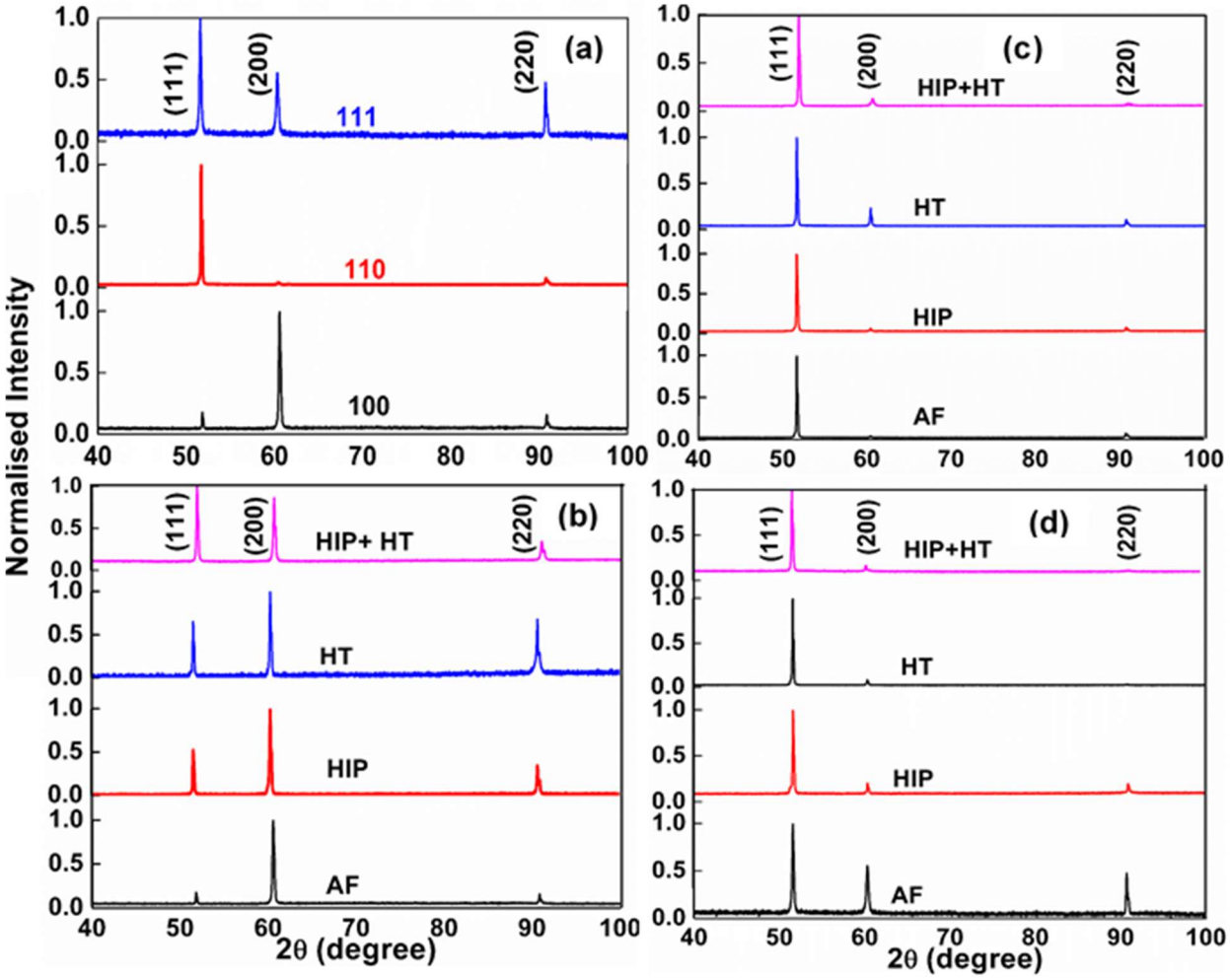

Fig. 7: Normalized XRD for (a) the AF 100, 110 and 111 samples, and (b,c and d) for the post-processed 100, 110 and 111 samples, respectively.

microstructure density [35] (See Fig.8a,b), which shows the closure of the defects in the AF sample following HIP without reopening again following the HT (See Fig.8c). In addition, there is a grain growth development from the columnar to the equiaxed shape for the AF samples following HIP and HT (See Fig.8d,e,f), in agreement with [27]. It is worth mentioning that the (111) texture in the 110 and 111 samples has been preserved and sometimes further strengthened after HIP and HT post-processes as seen in Fig. 7, and through calculating the texture coefficient (I_{200}/I_{111}) [36] in Fig.9.

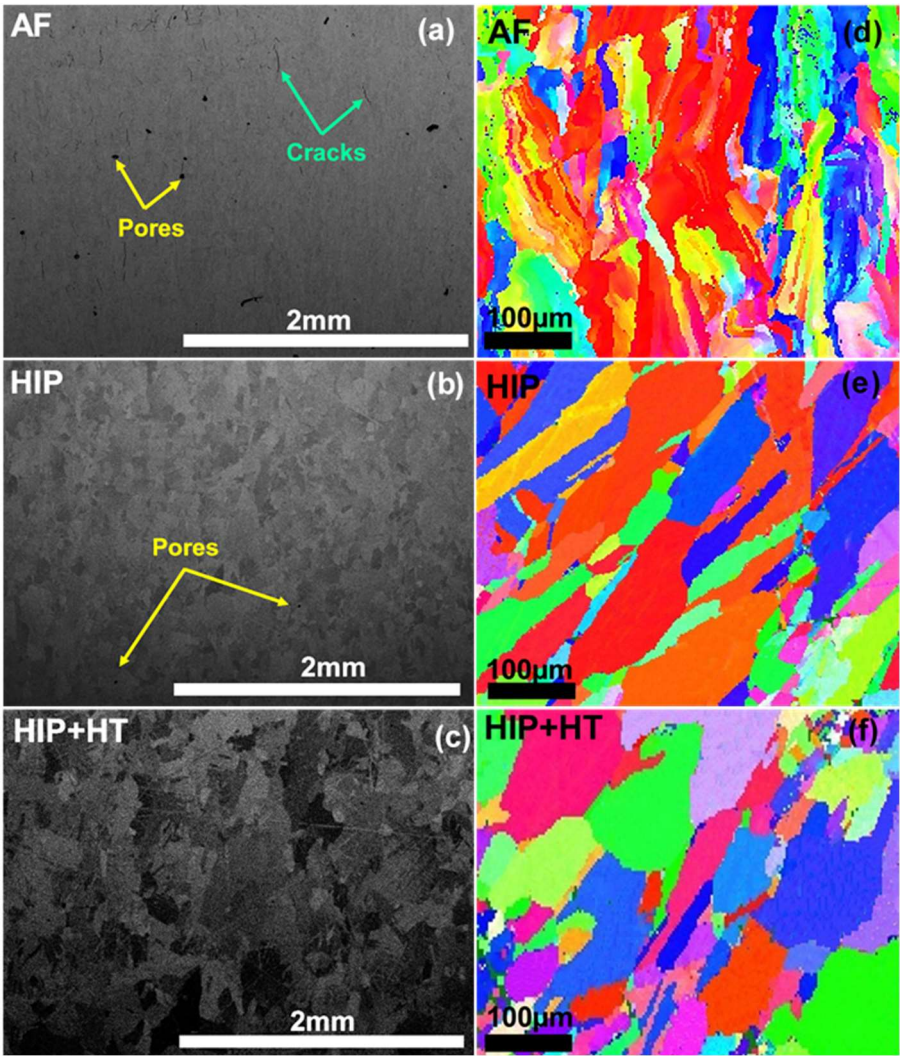

Fig.8: (a,b,c) SEM micrographs of the AF, HIP and HIP+HT conditions, respectively, of the 100 sample with E=4.68J/mm^2, and (d,e,f) their respective EBSD maps.

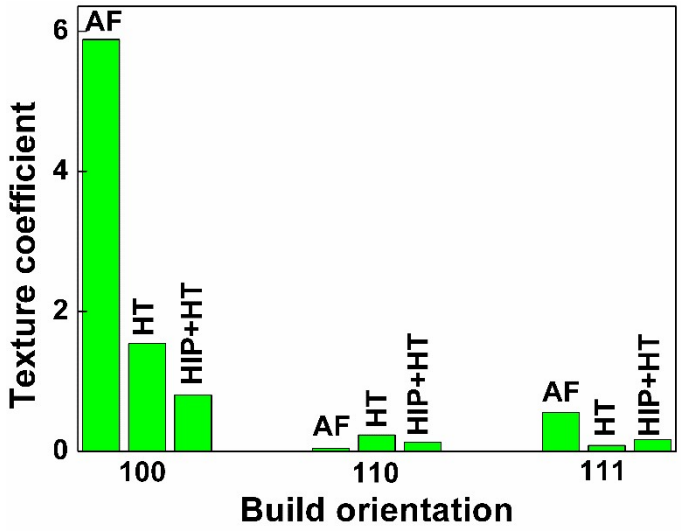

Fig.9: Texture coefficient (I_{200}/I_{111}) of the AF and post-processed 100, 110 and 111 oriented samples.

3.2.2 Magnetic properties

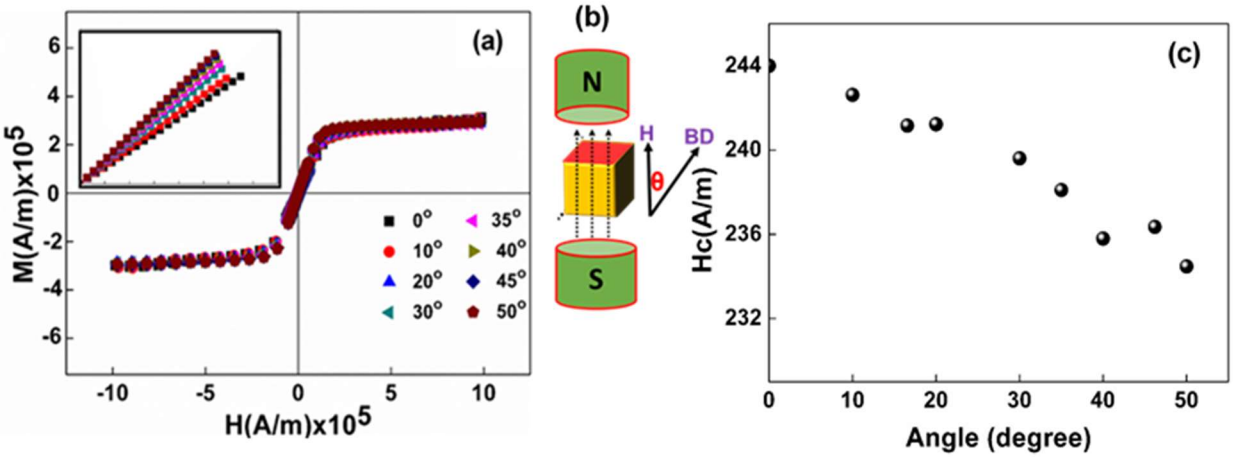

Fig.10: (a) Angular dependence of hysteresis loops of the AF 100 sample built with E=4.68J/mm^2, (b) a schematic represents the angle between the applied magnetic field and the build direction (BD), and (c) the determined angular dependence of coercivity of the AF 100 E=4.68J/mm^2 sample.

Fig.10a depicts the angular-dependent hysteresis loops of the AF 100 sample=4.68J/mm^2, where these measurements were performed by changing the angle θ between the applied magnetic field direction and the sample's build direction (BD) axis (see Fig.10b). **Fig.10a** illustrates the change in the slope of the initial magnetisation curves with θ (See the inset), meaning that the saturation magnetic field decreases with increasing θ. This is in agreement with [37] and confirms the dependence of magnetic anisotropy on the texture orientation. In addition, it is observed that H_c decreases slightly with the increase in θ [37]. The angular dependence of hysteresis loops and the extracted H_c reveals the change in magnetic anisotropy with grain orientation. **Fig. 11a** displays the hysteresis loops of the AF 100, 110 and 111 oriented samples. The magnetisation of AF 100 sample is saturated at a higher applied magnetic field (1.55x10^{5}A/m) than in the AF 110 and 111 oriented samples (0.82x10^{5}A/m and 0.8x10^{5}A/m, respectively) (see the inset of Fig.11a). And the H_c value of the AF 100 sample decreases from 242A/m to 230A/m and 228A/m with tilting the crystallographic orientation to the [110] and [111] directions, respectively. The decrease in saturation magnetic field and H_c values with changing the crystallographic orientation reveals a strong magnetic anisotropy and better soft magnetic properties that arise from changing the grain orientation (texture) from the

hard axis of magnetisation <100>, which is the preferred grain orientation direction of Mu-metal, to the easy axes of magnetisation of this alloy [4]. In addition, a promotion in the soft ferromagnetic behaviour is observed with the HT and HIP post-processes (see Fig.11b,c,d and Table 2), where M_s increases and H_c decreases following HIP and HT, which agrees with the results in Refs [4,27,38]. The decrease in H_c value with HIP and HT post-processes refers to the improvements of the microstructural defects, such as stress relief, defects closure, dislocations and inclusion elimination, which are the main resources of magnetic domain walls pining [39], in addition to the increase in grain size (see Fig. 8d,e,f) [40]. It is worth mentioning that the AF 100, 110 and 111 samples in Fig.11a show almost constant M_s value (see Table 2). This is because M_s is an intrinsic property that can be affected only by chemical composition [41], (magnetisation is the number of atomic magnetic moments in unit volume), and all samples in Fig.11a are the same alloy and processed with the same laser parameters. Meanwhile, the improvement in the M_s values with HIP and HT post-processes could arise from the change in the chemical composition of the alloy. The chemical analysis has shown the presence of oxides in the AF LPBF Ni-Fe-Mo as presented in Table 1. these oxides are formed during the LPBF process and have been identified as Mo, Si and Fe oxides as reported in our previous studies for this alloy by tunnelling electron microscopy (TEM), which are too small to be detected by XRD [4,6]. Such oxides decrease with the HT process in Hydrogen [4,6], returning Fe and Mo into the solid solution matrix, approaching the optimum chemical composition of the Mu-metal ($Ni_{80}Fe_{15}Mo_5$)[4,6] (See Table 1). This is confirmed by the thermal dependence of magnetisation measurements of the AF and HIP+HT conditions for the E=4.68J/mm^2 sample (100 orientation), which are presented in Fig.12. The AF condition shows a maximum magnetisation (M) and Curie temperature (T_c) values of 1.2x10^5 A/m and 425 ºC, respectively, which are improved with the following HIP+HT post-process to 1.42x10^5 A/m and 480 ºC, respectively, in agreement with [42, 43]. M and T_c are intrinsic magnetic properties

and their improvement with HIP and HT post-process arises from the improvement in grain size and chemical composition due to Fe and Mo immigration to the main matrix. It is worth mentioning that finishing post-processing with the HT instead of the HIP treatment results in better soft ferromagnetic properties (see Table 2), this is because HIP process, sometimes, doesn't result in a complete stress relief [44], in contrast with HT process in Hydrogen atmosphere that decreases oxides and reliving stresses [45].

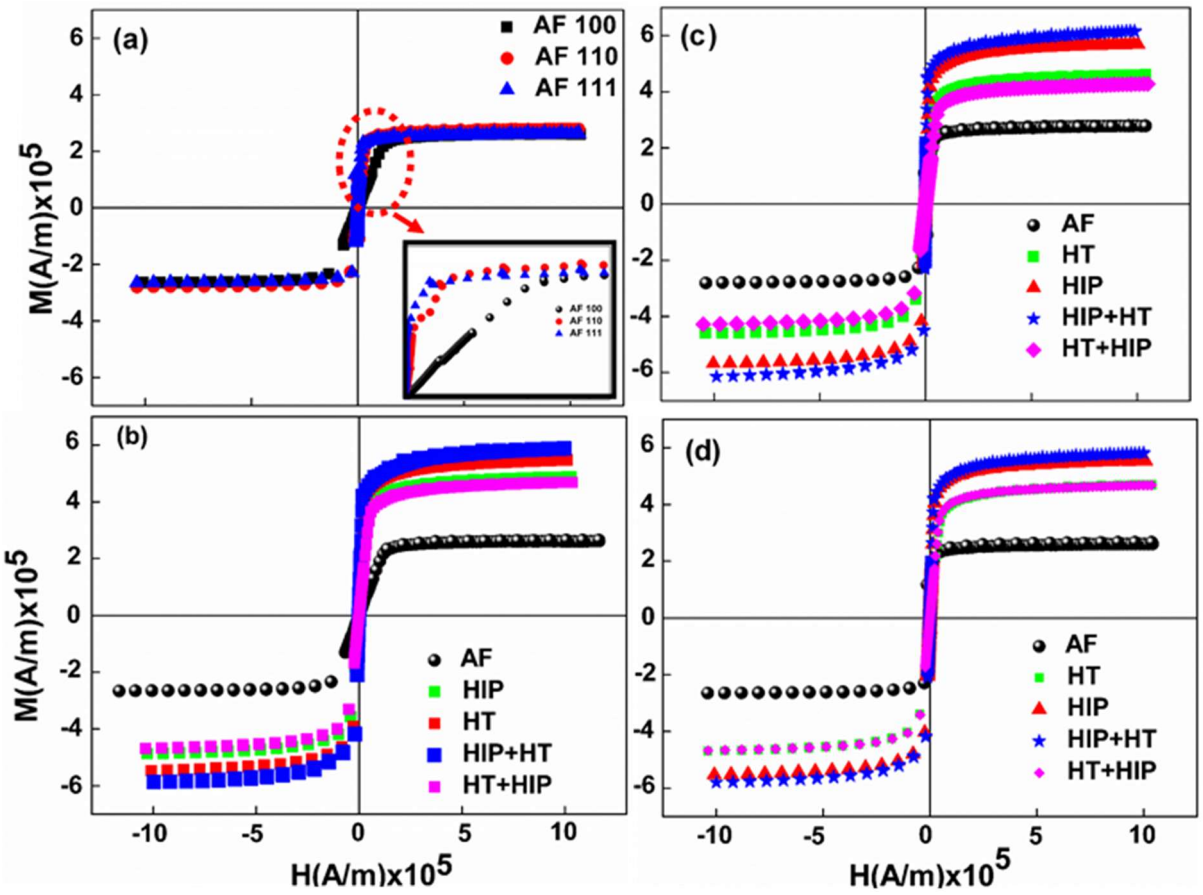

Fig. 11: Hysteresis loops of the sample with E=4.68J/mm^2 (a) AF sample at 100,110 and 111 orientations and (b,c,d) for the post-processed 100, 110 and 111 samples, respectively.

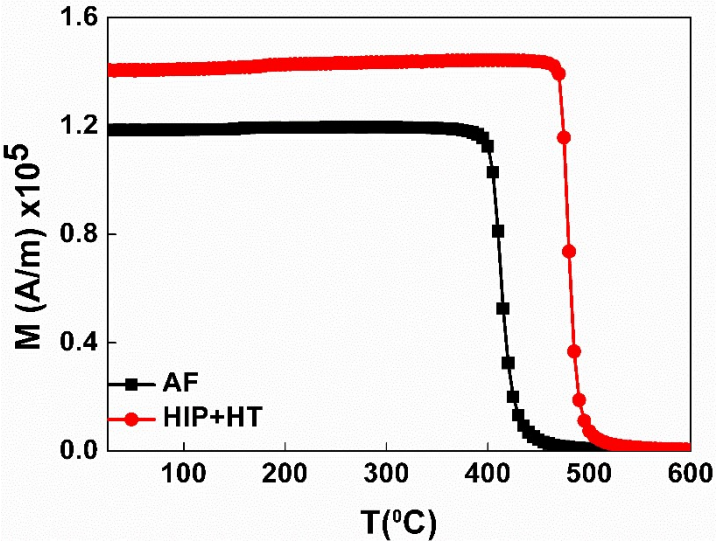

Fig 12: Thermal dependence of magnetisation of the AF and HIP+HT conditions for the E=4.68J/mm^2 sample (100 orientation) at 0.05T.

Table2: Saturation magnetisation and coercivity of the AF and post-processed HT and HIP samples built with E=4.68J/mm^2 at different orientations.

Orientation	Condition	Ms (A/m) x10^5	Hc(A/m)
[100] 0°	AF	2.36	242
	HT	4.45	232
	HIP	4.89	225
	HIP+HT	5.16	198
	HT+HIP	4.16	211
[110] 45°	AF	2.47	230
	HT	4.11	229
	HIP	5.09	228.5
	HIP+HT	5.51	194
	HT+HIP	3.72	204
[111] 35°	AF	2.43	228
	HT	4.21	224
	HIP	5.10	225
	HIP+HT	5.24	180
	HT+HIP	4.116	207

3.2.3 Magnetic shielding performance

Fig. 13 shows the axial and transverse magnetic shielding performance of the AF, HIP and HT post-processed 110 and 111 orientation tubes. Magnetic shielding arises from the magnetic flux shunting effect, a character of the magnetically permeable material [46]. The AF 110 and 111 samples do not show significant differences in the maximum axial/transverse SF values (SF_{max}), due to the microstructural defects, which impair the magnetic permeability (μ_r). The SF_{max} is significantly enhanced in both orientations following HIP and HT post-processes. However, the combination of both HIP and HT post-processes is found to be more effective in the improvement of the SF_{max} in both axial and transversal directions, rather than

the individual post treatment (see Fig.13). This is where the HIP+HT route achieves an average axial SF_{max} value of 124 for both 110 and 111 sample orientations, which is ten times the AF condition. The same improvement is observed in the transverse SF_{max}, however, the transverse SF_{max} values are higher, reaching 502 and 350 for the 110 and 111 orientations, respectively, which are 83% and 53% of the current commercial Mu metal, $Ni_{80}Fe_{15}Mo_5$, magnetic shields that shows SF of 600 [1,4]. The higher values of the transverse SF_{max} refers to the eddy current component that is getting higher in the transverse measurement and works against the externally applied magnetic field [47]. The promotion in the magnetic shielding performance, with HIP and HT post-processes, can be interpreted according to the enhancement in magnetic permeability (μ_r), due to the decrease in dislocation density, inclusions, stresses and the enhancement in grain size [48]. The grain size plays an important role in magnetic shielding via their influence on the eddy current, where, it is known that the eddy currents could be weakened with the increase in grain size, damping the magnetic shielding effect [49, 50]. This may explain the higher transverse SF_{max} value of the 110 sample than 111 sample, in the HIP+HT condition, where the HIP+HT 110 sample shows smaller grain size (in transverse direction), leading to less weakening in eddy currents, and accordingly a higher magnetic shielding effect [50] (See Fig.14). Meanwhile, both samples show almost the same grain size in the axial direction, leading to similar axial SF_{max} values. This will be further investigated to confirm the impact of grain morphology on magnetic shielding anisotropy.

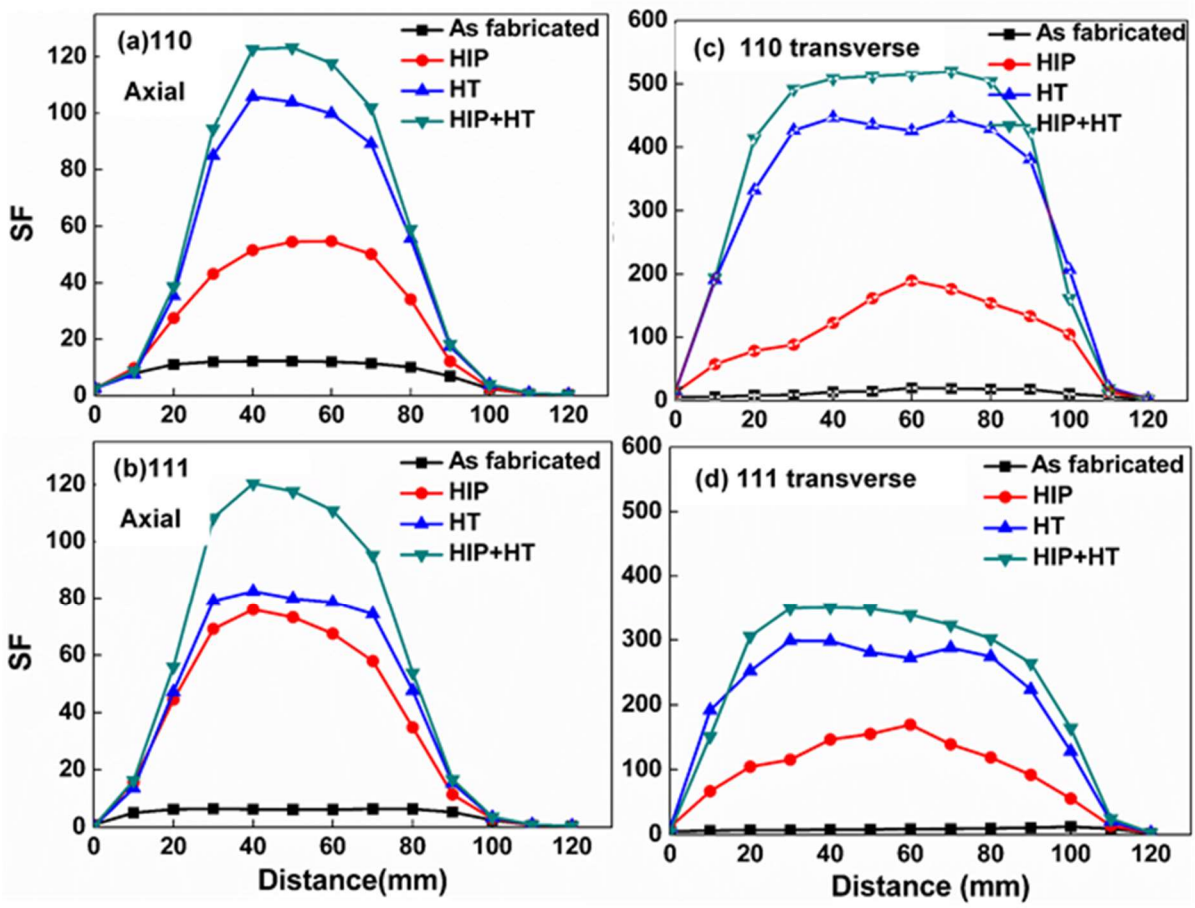

Fig. 13: The change of axial and transverse shielding factor with distance for the 110 and 111 orientations at different HT and HIP post-processes.

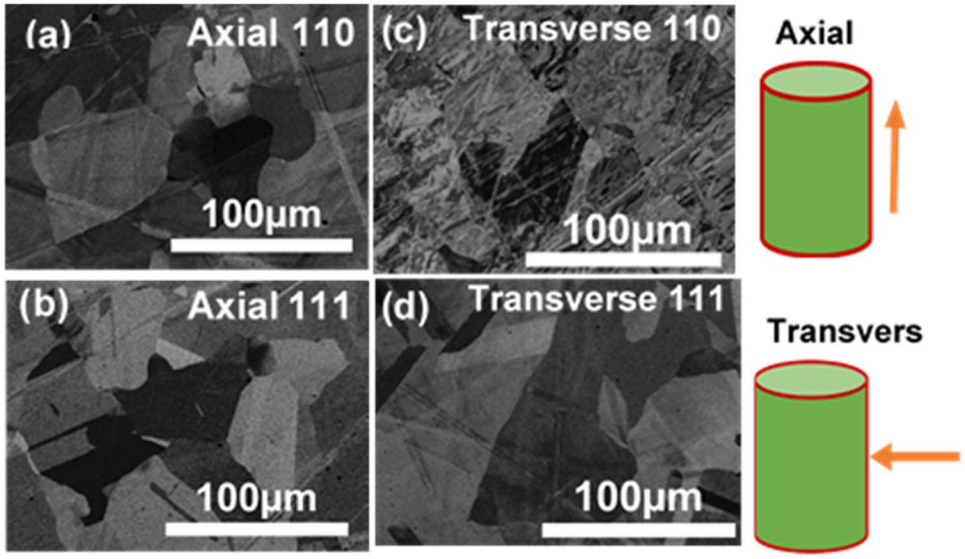

Fig.14: SEM micrographs of the HIP+HT condition of 110 and 111 tubes showing the grain structure, where (a,b) show the grain structure along the axial direction the axial direction, and (c,d) along transverse direction.

Conclusion

The Ni-Fe-Mo alloy was fabricated using the LPBF technique. The H_c values were optimised using a wide range of laser parameters. The AF sample with E=4.68J/mm^2 shows the lowest H_c of 242A/m and a microhardness value of 230HV. This sample was built with a tilted crystallographic orientation of 45º and 35º with respect to the build direction to control the magnetic anisotropy. The results show an improvement in the magnetic properties with tilting, due to releasing the grain growth in the easy axes magnetisation, which acquired further improvement with the HIP and HT post-processes. The [110] HIP+HT sample achieved H_c value of 194A/m and M_s value of 5.51 x 10^5A/m, and SF of 502, which is 83% of the commercial magnetic shields, confirming the ability of additive manufacturing to provide higher quality magnetic shields. However, further investigations are needed to match the needs of commercial.

Acknowledgment

The authors would like to acknowledge funding from EPSRC through the grants EP/M013294/1 and EP/R002789/1. The authors would like to acknowledge Mr. Eliot M. Dawson previously from Magnetic Shields Ltd. for providing the magnetic shielding measurements.

Author Contributions

AAM fabricated the samples and performed the magnetic properties measurements, assisted by RSS. AAM also performed HIP post-process, XRD, SEM, EBSD and hardness test. KB suggested the topic and identified the material performance requirements. MMA supervised the project on both the processing and material characterisation fronts. AAM wrote the paper with help from MMA. All authors reviewed the manuscript.

References

1- J. Vovrosh, Ge. Voulazeris, P. G. Petrov, J. Zou, Y. Gaber, L. Benn, D. Woolger, M. M. Attallah, V. Boyer, K. Bongs, M. Holynski, Additive manufacturing of magnetic

shielding and ultra-high vacuum flange for cold atom sensors, Scientific Rep. 8 (2018) 2023.

2- Boddice, D., Metje, N. & Tuckwell, G. Capability assessment and challenges for quantum technology gravity sensors for near surface terrestrial geophysical surveying. Journal of Applied Geophysics 146, 149–159 (2017)

3- J. Füzera, P. Kollár, D. Oleksáková, S. Roth, AC magnetic properties of the bulk Fe-Ni and Fe-Ni-Mo soft magnetic alloys prepared by warm compaction, J. Alloy Compd. 483 (2013) 557-559.

4- A. A. Mohamed, J. Zou, R. S. Sheridan, K. Bongs, M.M. Attallah, Magnetic shielding promotion via the control of magnetic anisotropy and thermal Post processing in laser powder bed fusion processed NiFeMo-based soft magnet, Additive Manufacturing 32 (2020) 101079.

5- B. Zhang, N. Fenineche, H. Liao, C. Coddet, Magnetic properties of in-situ synthesized FeNi3 by selective laser melting Fe-80%Ni powders, J. Magn. Magn. Mater. 336 (2013) 49-54.

6- J. Zou, Y. Gaber, G. Voulazeris, S. Li, L. Vazquez , L. F. Liu, M. Y. Yao, Y. J. Wang, M. Holynski, K. Bongs and M. M. Attallah, Controlling the grain orientation during laser powder bed fusion to tailor the magnetic characteristics in a Ni-Fe based soft magnet Acta Materialia 158 (2018) 230-238.

7- I. Chicinas, O. Geoffroy, O. Isnard, V. Pop, Soft magnetic composite based on mechanically alloyed nanocrystalline Ni3Fe phase, J. Magn. Magn. Mater. 290 (2005) 1531-1534.

8- P. Ripka, Sensors based on bulk soft magnetic materials: Advances and challenges, J. Magn. Magn. Mater. 320 (2008) 2466–2473.

9- H. Ali, H. Ghadbeigi and K.Mumtaz, Residual stress development in selective laser-melted Ti6Al4V: a parametric thermal modelling approach, The Inter. J. Adv. Manufacturing Techn.97 (2018) 262-2633.

10- H. H. Dastgerdi, M. O. Shabani and Y. Shajari, The Effect of Cooling Rate on the Solutionizing of IN718 Superalloy Produced via Selective Laser Melting (SLM) Method , J. Environmental Friendly Materials 3 (2019) 17-22.

11- A. B. Kustasa, D. F. Susan, K. L. Johnson, S. R. Whetten, M. A. Rodriguez, D. J. Dagel, J. R. Michael, D. M. Keicher, N.Argibay, Characterization of the Fe-Co-1.5V soft ferromagnetic alloy processed by Laser Engineered Net Shaping (LENS), Additive Manufacturing 21 (2018) 41-52.

12- L.N. Carter, X. Wang, N. Read, R. Khan, M. Aristizabal, K. Essa, M.M. Attallah, Process optimisation of selective laser melting using energy density model for nickel based superalloys, Mater. Sci. Techn. 32 (2015) 657-661.

13- T. Rikitake, Magnetic and Electromagnetic Shielding, TERRAPUB and D. Reidel Publ. Co., Tokyo, Dordrecht, 1987.

14- T. Boegelein, S.N. Dryepondt, A. Pandey, K. Dawson, G. Tatlock, Mechanical response and deformation mechanisms of ferritic oxide dispersion strengthened steel structures produced by selective laser melting, Acta. Mater. 87 (2015) 201-215.

15- L. van Belle, G. Vansteenkiste, and J. C. Boyer, Investigation of Residual Stresses Induced during the Selective Laser Melting Process, Key Eng. Mater., 554-557 (2013) 1828-1834

16- Neil J. Harrison, Iain Todd, Kamran Mumtaz, Reduction of micro-cracking in nickel superalloys processed by Selective Laser Melting: a fundamental alloy design approach, Acta Mater. 94 (2015) 59-68.

17- D. Tomus, T. Jarvis, X. Wu, J. Mei, P. Rometsch, E. Herny, Controlling the microstructure of Hastelloy-X components manufactured by selective laser melting, Phys. Proc. 41 (2013) 816-820

18- L. Zhou, T. Yuan, R. Li, J. Tang, G. Wang, K. Guo, Selective laser melting of pure tantalum: densification, microstructure and mechanical behaviors, Mater. Sci. Eng. A, 707 (2017). 443-451.

19- M. Cloots, P. J. Uggowitzer, K.Wegener, Investigations on the microstructure and crack formation of IN738LC samples processed by selective laser melting using Gaussian and doughnut profiles, Mater. Des. 89 (2016) 770-784.

20- M. M. Attallah, R. Jennings, X. Wang, L. N. Carter, Additive manufacturing of Ni-based superalloys: the outstanding issues, MRS Bull. 41 (2016) 758-764.

21- Q. Li, C. W. Kartikowati, S. Horie, T. Ogi, T. Iwaki, K. Okuyama, Correlation between particle size/domain structure and magnetic properties of highly crystalline Fe_3O_4 nanoparticles, Scientific Reports 7 (2017) 9894 .

22- B. Lu, M.Q. Huang, Q. Chen, B.M. Ma, D.E. Laughlin, Microstructure and magnetic domain structure of boron-enriched $Nd_2(FeCo)_{14}B$ melt-spun ribbons J. Magn. Magn. Mater. 195 (1999) 611-619.

23- I. Shishkovsky, V. Saphronov, Peculiarities of selective laser melting process for permalloy powder, Mater. Lett. 171 (2016) 208-211

24- B. Li, W. Fua, H. Xu, B. Qian, F. Xuan, Additively manufactured Ni-15Fe-5Mo Permalloy via selective laser melting and subsequent annealing for magnetic-shielding structures: Process, microstructural and soft-magnetic characteristics, J. Magn. Magn. Mater. 494 (2020) 165754.

25- C.V. Mikler, V. Chaudhary, V. Soni, B. Gwalani, R. V. Ramanujan, R. Banerjee, Tuning the phase stability and magnetic properties of laser additively processed Fe-30at%Ni soft magnetic alloys, Mater. Lett. 199 (2017) 88-92.

26- Y. Sato, T. Takeyama, Magnetic and mechanical properties of a 6% V permalloy as magnetic head materials, Trans. Jpn. Inst. Met. 26 (1985) 587-594.

27- M. Garibaldi , I. Ashcroft , N. Hillier , S.A.C. Harmon , R. Hague, Relationship between laser energy input, microstructures and magnetic properties of selective laser melted Fe-6.9%wt Si soft magnets, Mater. characterization 143 (2018) 144.

28- L Tonelli, E Liverani, G. Valli, A. Fortunato, L. Ceschini, Effects of powders and process parameters on density and hardness of A357 aluminum alloy fabricated by selective laser melting, The International Journal of Advanced Manufacturing Technology 106 (2020)371-383

29- D. Wang, C. Song, Y. Yang, Y. Bai, Investigation of crystal growth mechanism during selective laser melting and mechanical property characterization of 316L stainless steel parts, Materials and Design 100 (2016) 291-299.

30- W. M. Tucho, V. H. Lysne, H. Austbo, A. S. Kverneland, V. Hansen, Investigation of effects of process parameters on microstructure and hardness of SLM manufactured SS316L, J. Alloy Compds 740 (2018) 910-925.

31- S. Yusuf, Y. Chen, R. Boardman, S. Yang, N. Gao, Investigation on Porosity and Microhardness of 316L Stainless Steel Fabricated by Selective Laser Melting, Metals 7(2017)64.

32- P. V.Yekta, A.Ghasemi, E. M. Sharif, Magnetic and mechanical properties of cold-rolled permalloy, J.Magn.Magn. Mater. 468 (2018) 155-163.

33- Y. Karabulut, E. Tascioglu,YKaynak, Heat treatment temperature-induced microstructure, microhardness and wear resistance of Inconel 718 produced by

selective laser melting additive manufacturing, Optik, in press doi: https://doi.org/10.1016/j.ijleo.2019.163907.

34- X. Li, J.J. Shi, G.H. Cao, A.M. Russell, Z.J. Zhou, C.P. Li, G.F. Chen, Improved plasticity of Inconel 718 superalloy fabricated by selective laser melting through a novel heat treatment process, Mater. Design 180 (2019) 107915-107922.

35- K. Gupta, K.K. Raina, S.K. Sinha, Influence of process parameters and alloy composition on structural, magnetic and electrical characteristics of Ni-Fe permalloys, J. Alloy Compd. 429(2007) 357-364.

36- B. Attard, S. Cruchley, Ch. Beetz, M. Megahed, Y.L. Chiu, M.M. Attallah, Microstructural control during laser powder fusion to create graded microstructure Ni-superalloy components, Additive Manufacturing 36 (2020) 101432.

37- S. Raviolo, A. Pereirac, D. M. A. Jaimesb, J. Escrig, N. Bajales, Angular dependence of the magnetic properties of Permalloy nanowire arrays: A comparative analysis between experiment and simulation, J. Magn. Magn. Mater. 499 (2020) 166240.

38- Kh. Gheisari, J.T. Oh, S. Javadpour, The effect of heat treatment on the structure and magnetic properties of mechanically alloyed Fe-45%Ni nanostructured powders J. Alloy. Compds 509 (2011) 1020-1024.

39- Y. Ogata, H. Iwasaki, Y. Kubota, M. Yarnamoto, T. Iimura, T. Shinohara, Hot Isostatic Pressing in Oxygen of Ferrite Magnet, Phys. IV France 7 (1997) C1-309-C1-310.

40- B. L. Cushing, V. O. Golub, M. Henry, B. L. Oliva, E. Cook, C. W. Holmes, C. J. O'Connor, Effects of annealing on the magnetic properties, size and strain of gold-coated Permalloy nanoparticles, Nanotechnology 16 (2005) 1701-1706.

41- C. Li, H. Ruan, D. Chen, K. Li, D.Guo, B. Shao, Effect of heat treatment on the microstructure and properties of Ni based soft magnetic alloy, Microsc. Res. Tech. 2018;1–7, DOI: 10.1002/jemt.23038.

42- T. Waeckerlé, A. Demier, F. Godard, H. Fraisse, Evolution and recent developments of 80%Ni permalloys, J. Magn. Magn. Mater. 505 (2020) 166635.

43- A. F. Milone, I. Ortalli, G.P. Sordo, Curie Temperature of Ni-Fe Alloys in the Region (24-35)% Ni from Miissbauer Experiments, NUOVO CIN[ENTO, 1 (1982) 18.

44- J. S. Jesus, L. P. Borrego, J. A. M. Ferreira, J. D. Costa, C. Capela, Fatigue behavior of Ti6Al4V alloy components manufactured by selective laser melting subjected to hot isostatic pressing and residual stress relief, Fatigue Fract. Eng. Mater. Struct. 44 (2021)1916.

45- C. Li, H. Ruan, D. Chen, K. Li, D. Guo and B. Shao, Effect of heat treatment on the microstructure and properties of Ni based soft magnetic alloy Microsc. Res. Tech., 8 (2018) 1-7

46- D. Budker, D. F. Kimball, S. M. Rochester, V. V. Yashchuk, Nonlinear electro- and magneto-optical effects related to Bennett structures, Phys. Rev. A 65 (2002) 033401-033407.

47- S.Y. Lee, Y.S. Lim, I.H. Choi, D.I. Lee, S.B. Kim, Effective Combination of Soft Magnetic Materials for Magnetic Shielding, IEEE Trans. Magn. 48 (2012) 4550-4553.

48- W. D. Kehr, Influence of Annealing Environments on the Permeability of 4-79 Molybdenum Permalloy, J. Appl. Phys. 41 (1970) 1857-1858.

49- M. De Campos, J. Teixeira, F. Landgraf, The optimum grain size for minimizing energy losses in iron, J. Magn. Magn. Mater. 301 (2006) 94-99.

50- T. Shimazu and M. Shiozaki, Effect of grain size and frequency on eddy current loss in Si-Fe Sheets, IEEE Transactions on Magnetics, 26 (1990) 1972.